AGU PUBLICATIONS

JGR

Journal of Geophysical Research: Space Physics

RESEARCH ARTICLE
10.1002/2017JA024464

Key Points:
- A neural-network-based 3-D dynamic electron density model is developed in the inner magnetosphere
- The DEN3D model successfully reproduced the quiet time structure, plasmaspheric erosion, and refilling and plume formation
- Long-term density variations are consistent with expectations, while short-term variations are modulated by substorm activity or enhanced convection

Correspondence to:
X. Chu,
chuxiangning@gmail.com

Citation:
Chu, X., et al. (2017), A neural network model of three-dimensional dynamic electron density in the inner magnetosphere, *J. Geophys. Res. Space Physics*, *122*, 9183–9197, doi:10.1002/2017JA024464.

Received 12 JUN 2017
Accepted 11 AUG 2017
Accepted article online 14 AUG 2017
Corrected 25 SEP 2017
Published online 2 SEP 2017

This article was corrected on 25 SEP 2017. See the end of the full text for details.

A neural network model of three-dimensional dynamic electron density in the inner magnetosphere

X. Chu[1], J. Bortnik[1], W. Li[1,2], Q. Ma[1,2], R. Denton[3], C. Yue[1,4], V. Angelopoulos[5], R. M. Thorne[1], F. Darrouzet[6], P. Ozhogin[7,8], C. A. Kletzing[9], Y. Wang[10], and J. Menietti[9]

[1]Department of Atmospheric and Oceanic Sciences, University of California, Los Angeles, California, USA, [2]Center for Space Physics, Boston University, Boston, Massachusetts, USA, [3]Department of Physics and Astronomy, Dartmouth College, Hanover, New Hampshire, USA, [4]University Corporation for Atmospheric Research, Boulder, Colorado, USA, [5]Department of Earth, Planetary, and Space Sciences, University of California, Los Angeles, California, USA, [6]Royal Belgian Institute for Space Aeronomy (BIRA-IASB), Brussels, Belgium, [7]Center for Atmospheric Research, University of Massachusetts Lowell, Lowell, Massachusetts, USA, [8]National Grid, Waltham, Massachusetts, USA, [9]Department of Physics and Astronomy, University of Iowa, Iowa City, Iowa, USA, [10]Goddard Planetary Heliophysics Institute, University of Maryland, Baltimore County, Baltimore, Maryland, USA

Abstract A plasma density model of the inner magnetosphere is important for a variety of applications including the study of wave-particle interactions, and wave excitation and propagation. Previous empirical models have been developed under many limiting assumptions and do not resolve short-term variations, which are especially important during storms. We present a three-dimensional dynamic electron density (DEN3D) model developed using a feedforward neural network with electron densities obtained from four satellite missions. The DEN3D model takes spacecraft location and time series of solar and geomagnetic indices ($F_{10.7}$, *SYM-H*, and *AL*) as inputs. It can reproduce the observed density with a correlation coefficient of 0.95 and predict test data set with error less than a factor of 2. Its predictive ability on out-of-sample data is tested on field-aligned density profiles from the IMAGE satellite. DEN3D's predictive ability provides unprecedented opportunities to gain insight into the 3-D behavior of the inner magnetospheric plasma density at any time and location. As an example, we apply DEN3D to a storm that occurred on 1 June 2013. It successfully reproduces various well-known dynamic features in three dimensions, such as plasmaspheric erosion and recovery, as well as plume formation. Storm time long-term density variations are consistent with expectations; short-term variations appear to be modulated by substorm activity or enhanced convection, an effect that requires further study together with multispacecraft in situ or imaging measurements. Investigating plasmaspheric refilling with the model, we find that it is not monotonic in time and is more complex than expected from previous studies, deserving further attention.

1. Introduction

The plasmasphere is a region of cold dense plasma in the inner magnetosphere, extending from Earth's upper atmosphere to the plasmapause [*Carpenter*, 1966; *Nishida*, 1966; *Lemaire et al*., 1998; *Darrouzet et al*., 2009]. During geomagnetically quiet times, the plasmasphere is populated by ions and electrons in dynamic equilibrium with the upper ionosphere. During active times, such as geomagnetic storms, the plasmasphere is eroded by enhanced magnetospheric convection, which results in a contraction of the plasmapause to lower *L* shells. The plasmasphere in the afternoon region is drawn toward the dayside magnetopause, forming a plume [*Grebowsky*, 1970; *Ober et al*., 1997; *Goldstein et al*., 2004; *Darrouzet et al*., 2008]. During the storm recovery phase, low-energy ionospheric plasma is drawn upward from low altitudes along magnetic field lines, refilling regions that were previously emptied by storm time convection. The plasmasphere is constantly in a dynamic state, with erosion occurring on a time scale of a few hours in response to increasing geomagnetic activity and subsequent refilling, occurring over a few days during quiet times [*Kersley and Klobuchar*, 1980; *Dent et al*., 2006; *Sandel and Denton*, 2007; *Foster et al*., 2014].

Several empirical models have been developed in previous studies to statistically describe the plasma density (or electron number density) in the equatorial plane [*Carpenter and Anderson*, 1992; *Sheeley et al*., 2001] and along magnetic field lines [*Gallagher et al*., 2000; *Denton et al*., 2002a, 2002b, 2004; *Tu et al*., 2006; *Reinisch et al*., 2009; *Ozhogin et al*., 2012]. Regarding the equatorial plasma density, it is usually modeled with two separate empirical functions for the trough and plasmaspheric regions, respectively, and a function for the

plasmapause location. The empirical functions for the trough and plasmaspheric densities are expressed in the form of either exponential or power law functions or a mix of the two [*Carpenter and Anderson*, 1992; *Sheeley et al*., 2001]. They depend on L shell and are usually independent of time and geomagnetic activity [*Sheeley et al*., 2001] and weakly dependent on long-term solar cycle effects and seasonal effects [*Carpenter and Anderson*, 1992]. To resolve the dynamic evolution of the plasmasphere such as storm time erosion and refilling on a time scales as short as a few hours, *Bortnik et al*. [2016] and *Chu et al*. [2017] have developed a time-dependent equatorial plasma density model using a neural network approach with time series of solar and geomagnetic indices as model inputs. The neural network model successfully reconstructed various density features and dynamic behavior, such as the quiet time plasmasphere, erosion, and recovery of the plasmasphere, as well as plume formation during a storm.

In addition to empirical models describing the equatorial electron density, the field-aligned distribution has been investigated with different approaches and data sets. In the global core plasma model (GCPM) [*Gallagher et al*., 2000], the field-aligned density profiles were obtained by interpolating between the topside ionospheric profile of International Reference Ionosphere model and the equatorial plasmaspheric density profiles [*Carpenter and Anderson*, 1992] using an exponential function. Later, field-aligned electron density distributions were studied using in situ observations from the plasma wave instrument onboard the Polar satellite [*Goldstein et al*., 2001; *Denton et al*., 2002a, 2002b]. The field-aligned plasma density was assumed a power law function, for instance, $n_e = n_{e0}\left(\frac{LR_E}{R}\right)^{\alpha} = n_{e0}\sec\lambda^{2\alpha}$, where n_{e0} is the electron density at the equator, L is the L shell, R_E is the radius of the Earth, R is the geocentric distance from the Earth's center, λ is the magnetic latitude (MLAT), and α is a function of L shell. The parameter α was fitted when a polar-orbiting satellite crossed the same L shell under the assumption of no magnetic local time (MLT) and temporal variations. Besides using in situ measurements, the field-aligned plasma density distribution was also directly obtained using echo observations from the radio plasma imager (RPI) onboard the IMAGE satellite [*Reinisch et al*., 2001; *Huang et al*., 2004; *Tu et al*., 2006; *Ozhogin et al*., 2012]. Additionally, the field-aligned electron density was occasionally obtained simultaneously in both hemispheres. The field-aligned plasma density was usually expressed in a slightly different composite form, $n_e = n_{e0}\cos^{-\beta}\left(\frac{\pi}{2}\frac{\alpha\lambda}{\lambda_{inv}}\right)$, where n_{e0} is the equatorial electron density, λ is the magnetic latitude, and λ_{inv} is the magnetic invariant latitude. The parameters α and β, which control the flatness and the steepness of the field-aligned density profiles, respectively, were fitted for specific events [*Huang et al*., 2004; *Reinisch et al*., 2004] and statistically [*Ozhogin et al*., 2012].

Most previous empirical electron density models were expressed as a function of L shell and had neither MLT dependence nor time dependence (i.e., geomagnetic activity dependence). However, a time-dependent model of the electron density is important for a variety of applications. For instance, plasmaspheric density and composition, which vary significantly at different levels of geomagnetic activity, strongly influence wave growth and propagation and energetic particle scattering [*Bortnik et al*., 2007; *Millan and Thorne*, 2007]. As a specific example, using in situ electron density obtained from the Van Allen Probes instead of a statistically averaged empirical model, *Thorne et al*. [2013] showed a much better comparison between modeled and observed electron acceleration during a major radiation belt enhancement event on 8–9 October 2012. However, satellite observations of electron densities are limited and not available for every storm event. Furthermore, it is the global distribution of the electron density, rather than the in situ density, that is required for modeling wave-particle interactions, since electron acceleration takes place over an extended path along the electrons' drift orbit at locations other than where the fortuitous in situ density measurements are obtained. Therefore, a time-dependent (i.e., geomagnetic activity-dependent) and global model of the electron density is essential.

Here we present such a three-dimensional dynamic electron density (DEN3D) model in the inner magnetosphere with a neural network approach. We describe the electron density data from several satellites used in this study, followed by a modeling methodology. Comprehensive comparisons between the observed and modeled electron density data are then performed. As an example, our model is used to simulate the densities during a geomagnetic storm on 1 June 2013. We show that the modeled 3-D density distribution can be used effectively to study the erosion and recovery of the plasmasphere during the geomagnetic storm. Our current neural network model is available (xnchu.github.io).

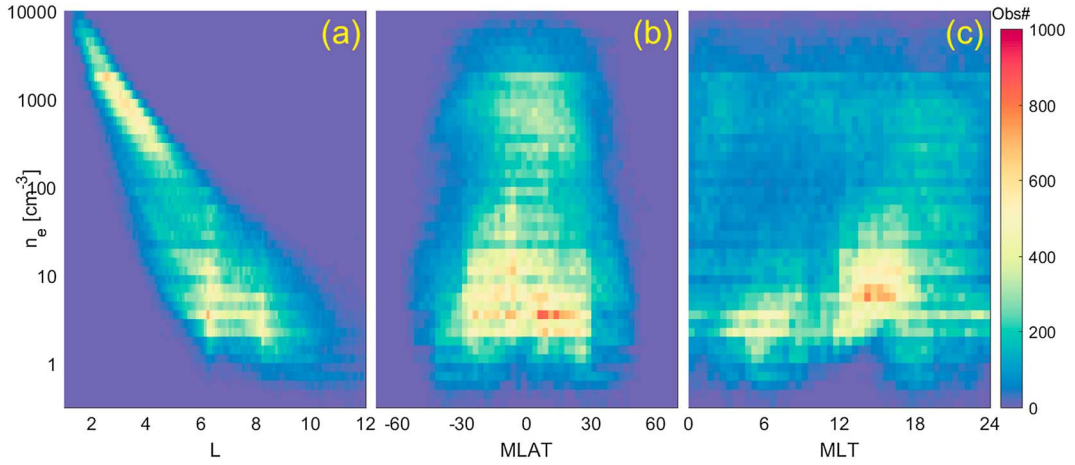

Figure 1. The distributions of in situ observations of the electron density $\log_{10}(n_e)$ with respect to (a) *L* shell (between 1 and 12), (b) MLAT (between −60° to 60°), and (c) MLT. The bin sizes are 0.1 for the L shell, 2.5 for MLAT, 0.5 for MLT, and 0.1 for the electron density. The colorbar shows the number of observations in each bin.

2. Database

In this study, we developed a three-dimensional dynamic electron density (DEN3D) model using in situ electron density, which was inferred from the upper hybrid resonance frequency or the plasma frequency identified from the continuum edge from the instruments onboard four satellites. The data from the four instruments: the plasma wave experiment onboard ISEE (27 October 1977 to 25 September 1987) [*Gurnett et al.*, 1978], the plasma wave experiment onboard CRRES (1 August 1990 to 13 October 1991) [*Anderson et al.*, 1992], the plasma wave instrument onboard Polar (26 March 1996 to 17 September 1997) [*Gurnett et al.*, 1995], and the radio plasma imager (RPI) onboard IMAGE (1 January 2001 to 19 December 2005) [*Reinisch et al.*, 2000]. The temporal resolution is reduced to 5 min averages to save computation time, which resulted in 217,500 data points in total (12%, 42.5%, 7.4%, and 38.1% from the four spacecraft, respectively). The *L* shell, MLT, and magnetic latitude (MLAT) of the in situ measurements are obtained in the solar magnetic coordinate system and traced along magnetic field lines computed using the Tsyganenko model T05 [*Tsyganenko and Sitnov*, 2005]. The relative error of the electron density derived from the wave measurements is typically less than 20% [*Reinisch et al.*, 2004] depending on the frequency resolution of the wave instrument. The consistency among the four data sets is checked in section 3.3.

Figure 1 shows the number of in situ observations of the electron density with respect to *L* shell, MLAT, and MLT. Figure 1a illustrates the number of observations versus the electron density n_e and *L* shell. At lower *L* shells between 1.5 and 4, the distribution of in situ densities is rather concentrated and the typical density values decrease linearly with respective to the *L* shell. This is consistent with power law and exponential functions used in previous empirical models [*Carpenter and Anderson*, 1992; *Sheeley et al.*, 2001]. The distribution extends toward lower density values at higher *L* shells that usually correspond to the trough region, where the distribution is more spread. Since our model focuses on the inner magnetosphere, we have limited our data set by using in situ observations within an *L* shell of 8. Figure 1b shows the number of in situ observations versus $\log_{10}(n_e)$ and MLAT. The measurements are centered around the equator and confined below $|\text{MLAT}| < 60°$. Figure 1c shows the number of in situ observations versus $\log_{10}(n_e)$ and MLT. The current database of the electron density covers all MLTs. The measurements of higher densities ($\log_{10}(n_e) > 2$) is rather uniform, while there are slightly more observations of lower densities ($\log_{10}(n_e) < 2$) in the afternoon sector between 12 and 18 MLT due to satellite orbits.

3. DEN3D Model

3.1. Model Description

Artificial neural networks (ANNs) are generic and convenient models used to represent complicated nonlinear functions. The ANN offers a number of advantages over conventional statistical fitting in developing

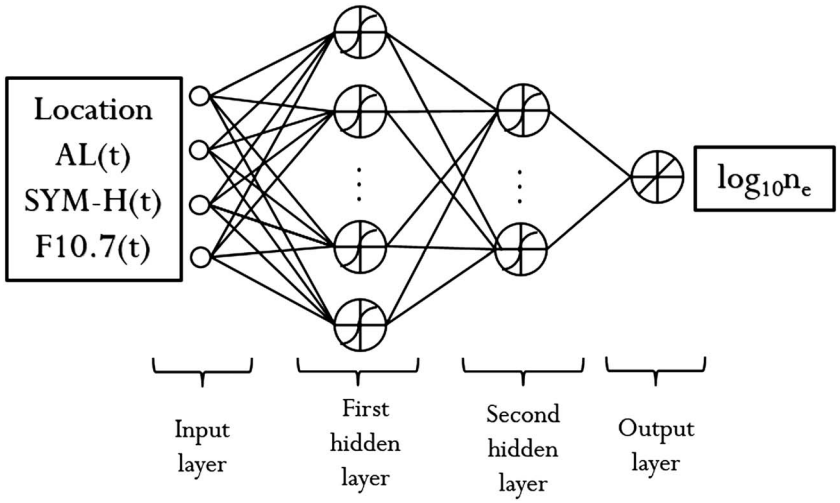

Figure 2. Architecture of the neural network model, with 60 and 10 neurons in the first and second hidden layers, respectively. The input parameters include the locations of the measurements (*L* shell, MLT, and MLAT), geomagnetic indices (*SYM-H* and *AL*), and solar EUV index ($F_{10.7}$). The target parameter is the logarithm of the electron density, $\log_{10}(n_e)$.

a three-dimensional dynamic electron density model. For instance, the dynamics of the electron density are very complex and depend on various factors. Implementing these dependences analytically requires a number of simplifying assumptions that may inadvertently suppress important physical interactions. These assumptions can be avoided by using a neural network (see section 5 for details).

In this study, we adopt a simple feedforward neural network consisting of two hidden layers to build our DEN3D model. Figure 2 shows the architecture of the neural network used for the DEN3D model, with 60 and 10 neurons in the first and second hidden layers, respectively. The architecture of the neural network is similar to those in previous studies which succeeded in modeling global dynamic distributions of the equatorial plasma density [*Bortnik et al.*, 2016; *Chu et al.*, 2017]. As shown in Figure 2, the inputs used for each neuron are the products of the output of preceding nodes with their associated weights $z_j^l = f\left(\sum_{i=0}^{N-1} z_i^{l-1} w_{ij} + b_i\right)$, where i and j denote the neuron number in the preceding and current layers, respectively, and w_{ij} and b_i are the weights and biases in the hidden layer. The output of each neuron in the hidden layers is calculated using a sigmoid activation function $f(z^l) = 1/(1+\exp(-z^l))$, which is commonly used for regression. The outputs of the preceding neurons are used as the inputs of the neurons in the next layer. The DEN3D model is trained using scaled conjugate gradient backpropagation to minimize the mean square error (MSE) of the logarithm of the electron density $\log_{10}(n_e)$, with 70% of the database randomly chosen as the training set, 15% as the validation set, and 15% as the test set. The training process continues to update the weights and biases until the cost of the validation set stops improving for several consecutive steps (here we chose 25 steps empirically in this study). These criteria of early stopping are widely used to avoid overfitting and improve the generalizability of the DEN3D model. The MSE of the test data set, which has never been "seen" by the model, can be used as an indicator of its out-of-sample performance (or the ability to predict).

The target of the DEN3D model is the logarithm of the electron density $\log_{10}(n_e)$. The input parameters include the locations of the measurements (*L* shell, MLT, and MLAT), geomagnetic indices *SYM-H* (ring current strength) and *AL* (lower envelope of the auroral electrojet indices), and solar index $F_{10.7}$ (solar radio flux). These indices are obtained from the OMNI database. We used time series of these indices rather than instantaneous values because the state of the plasmasphere heavily depends on its preceding states. We used the *SYM-H* index with 30 min resolution for the preceding 3 days, *AL* index with 10 min resolution in the preceding 5 h which covers the lengths of most substorms [*Chu et al.*, 2015, Figure 7], and daily $F_{10.7}$ index in the preceding 3 days. Therefore, the DEN3D model is not only time-dependent but also history-dependent. The variations of the modeled electron density are spatially and temporally continuous rather than stepwise discontinuous since the variations of the *SYM-H* and *AL* indices are smooth compared to the *Kp* index.

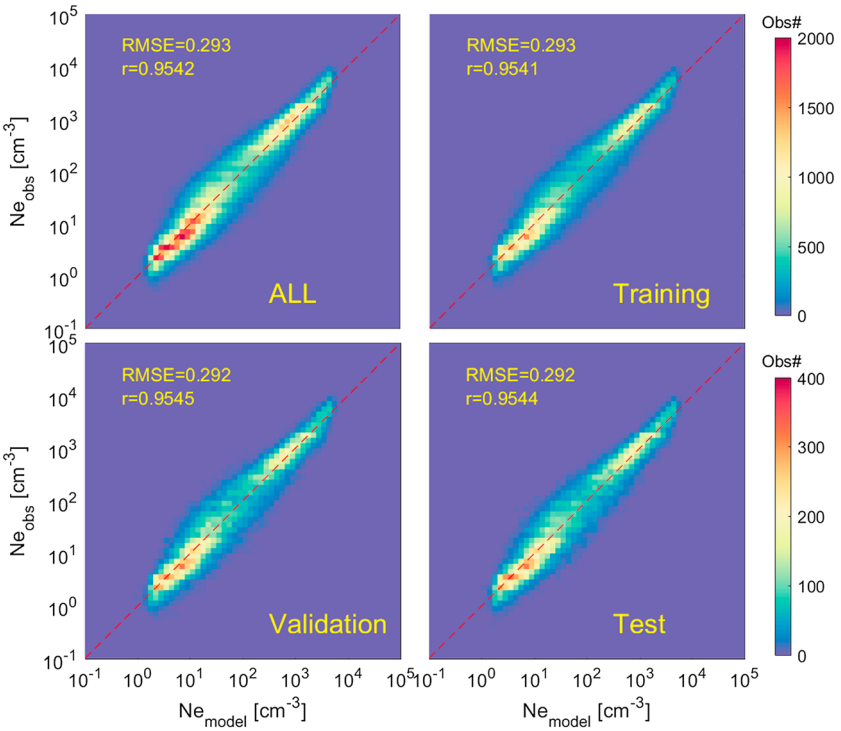

Figure 3. Correlation between the observed in situ electron density and predicted values by the neural network model for four data sets (all, training, validation, and test). The bin size is 0.1 for both the observed and modeled densities in all plots. The colorbar indicates the number of observations in each bin. The red dashed line is the diagonal indicating perfect agreement ($y = x$). The correlation coefficients r and RMSE are shown in the top left corners.

3.2. Model Performance

Figure 3 shows the correlation between the observed and modeled electron densities for the whole, training, validation, and test data sets. The colorbar shows the number of data points in each bin (note that the scales are different for top and bottom figures). The dashed line is the diagonal ($y = x$) on which there is perfect agreement between the observations and modeled values. Most data points are centered around the diagonal for all data sets, which indicates that most observations can be accurately modeled. The correlation coefficients r of all four data sets are close to 0.954. The correlation coefficient of the whole data set is 0.9542, which means that the neural network can explain r^2 = ~91% of the observed variability. The correlation coefficient is 0.9545 on the test data set. Since the test data set is not used in the training process, it suggests that the DEN3D model has good capability to make out-of-sample prediction. The root-mean-square error (RMSE) on the test data set of $\log_{10}(n_e)$ is 0.292, which can be translated to a factor of $10^{0.292} = 1.96$. It suggests that the neural network model can predict out-of-sample observations with the error around a factor of 2. All facts above demonstrate the excellent capabilities of the neural network model in reproducing the electron density.

3.3. Spacecraft Intercalibration

Intercalibration among multiple instruments onboard different spacecraft is essential to obtain accurate and consistent measurements of the electron density (and other parameters too), especially since these spacecraft are in different orbits and span different orbital periods. In addition, the analysis of intercalibration among these spacecraft plays an important role in providing accurate and consistent measurements to train a neural network. In general, intercalibration is a process that calibrates target instruments to a more accurate reference instrument by matching measurements in conjugate time, space, wavelength, etc. A major challenge for intercalibration is to find and acquire matched measurements. This is extremely difficult as our database of the electron density is obtained from multiple instruments onboard both polar-orbiting and equatorial orbiting spacecraft. In this study, we compared the observed and modeled densities for each spacecraft to check the consistency among these data sets.

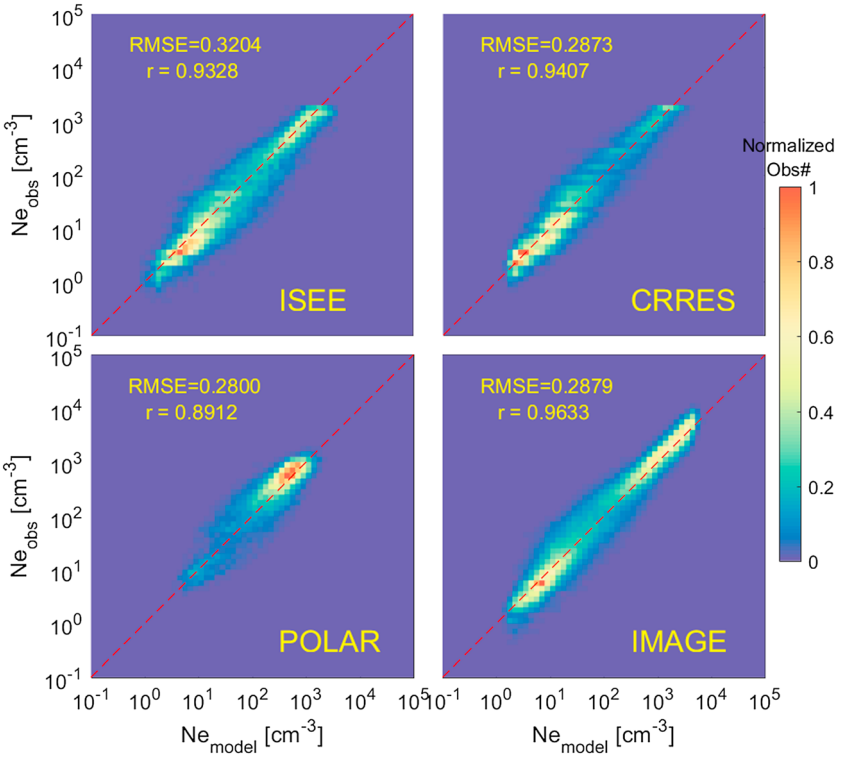

Figure 4. Correlation between the observed and modeled electron densities for four spacecraft (ISEE, CRRES, Polar, and IMAGE). The bin size is 0.1 for both the observed and modeled densities in all plots. The colorbar indicates the number of observations in each bin normalized by the maximum of bin values for each spacecraft. The red dashed line is the diagonal indicating perfect agreement ($y = x$). The correlation coefficients r and RMSE are shown in the top left corners.

Figure 4 shows the correlations between the measured and modeled electron densities for each spacecraft. For better visualization, we have normalized the data distribution by the maximum bin values for each spacecraft. The dashed line is the diagonal ($y = x$). As shown in Figure 4, the modeled densities are centered around the diagonal, indicating that the performance of the DEN3D model on each spacecraft is similar. The RMSE for the four spacecraft are all close to 0.30, and the correlation coefficients are greater than 0.90. The fact that no significant biases were present suggests that the electron densities from each spacecraft do not have significant offsets. This is expected since the relative errors of the electron densities obtained from these wave measurements are usually very small. It suggests good intercalibration among the electron densities obtained from the wave instruments onboard the four spacecraft. Therefore, no further calibration is required for the current study. It should be pointed out that a stricter way to test spacecraft intercalibration is to predict the electron densities from one spacecraft using a neural network model that is trained from three other spacecraft. This is, however, not practical for the current study because it results in four different models trained using incomplete data sets. The goal of our study is, however, to provide one single plasma density model trained using all spacecraft data sets.

3.4. Comparison With Empirical Density Models

Figure 5 shows the error distribution versus L shells for various empirical models of electron densities, including the DEN3D model, Ozhogin model [*Ozhogin et al.*, 2012], global core plasma model (GCPM) [*Gallagher et al.*, 2000] (version 2.4 from https://plasmasphere.nasa.gov/), and Denton model [*Denton et al.*, 2004, 2006] on the whole data set. The error is defined as the difference between the logarithms of the observed electron densities and the modeled values $\log_{10} n_{eobs} - \log_{10} n_{emodel}$. Note that the error distribution of the Ozhogin model is limited to within the plasmasphere using O'Brien's plasmapause model [*O'Brien and Moldwin*, 2003] and densities above 100 cm^{-3}. The mean errors of the neural network model are close to zero, and the RMSEs are small (around 0.3), suggesting good performance on the whole data set. The error distribution is similar for the whole, training, validation, and test data sets (not shown). The RMSE is also

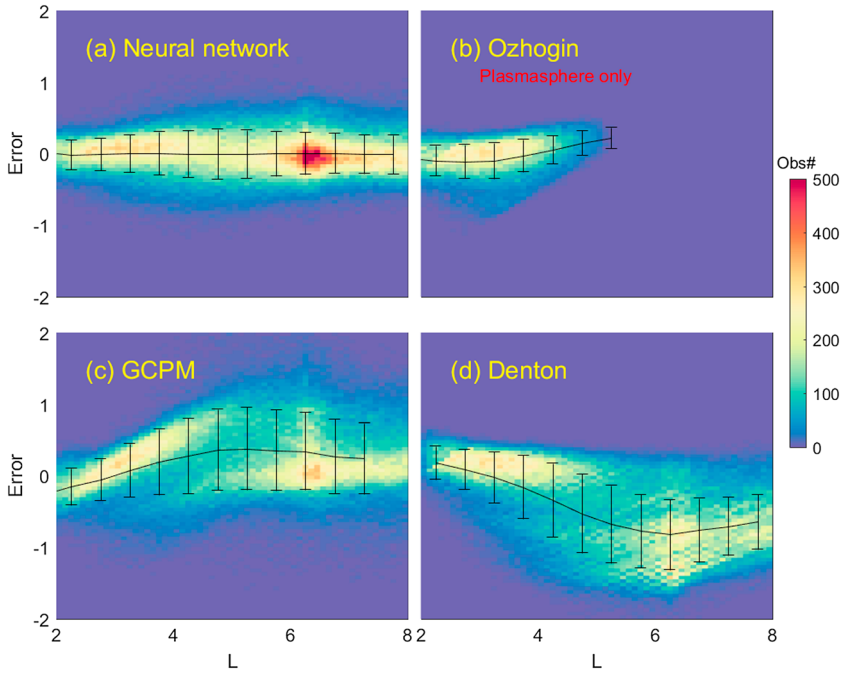

Figure 5. The error distributions as a function of *L* shell for (a) the neural network model, (b) the Ozhogin model, (c) the global core plasma model, and (d) the Denton model. The error is defined as the difference between the logarithms of the observed electron densities and the modeled values $\log_{10} n_{eobs} - \log_{10} n_{emodel}$. The bin sizes are 0.1 for the L shell and 0.05 for the error. The error bars illustrate the mean errors and RMSE as a function of *L* shell for four models.

fairly uniform versus L shell. It is, however, slightly lower at lower *L* shells since the density variations are small in the plasmasphere. The RMSE distribution as a function of *L* shell can be used to roughly estimate the uncertainty on a prediction by the DEN3D model.

The other empirical models do well in reproducing the plasmaspheric densities, since the RMSE is usually small at low *L* shells. They are, however, biased relative to our current data set to some degree. For example, the errors of the GCPM model have two populations: one population at lower *L* shell that underestimates the observations and another population at higher *L* shells that overestimates the observations. The two populations likely correspond to errors of the plasmaspheric (at lower *L* shell) and trough (at high *L* shell) regions, respectively. The biases of the plasmaspheric errors become as large as 1.0 near L ~ 4, which corresponds to error of a factor of 10. It should be noted that the DEN3D model is obtained using the current data set, while the other models are obtained using different instruments on different satellites, during different phases of solar cycles, and using different methods. Thus, our DEN3D model is expected to have better performance on the current data set, on which it is trained. In other words, this is not a completely fair comparison. Our focus, however, in addition to better performance, is the capability of the DEN3D model in reproducing the dynamic features of the plasmasphere.

3.5. Out-of-Sample Prediction

The DEN3D model is not only capable in reproducing plasma densities as shown above but also in predicting out-of-sample data. In this section, we show that the DEN3D model can predict electron density profiles along field lines that are not included in the training process of the neural network. The RPI onboard the IMAGE satellite provides not only in situ electron density inferred from upper hybrid resonance frequency but also instantaneous (typically within 1 min) electron density profiles along a magnetic field line inferred from the echo traces in the RPI active sounding plasmagrams [*Burch et al.*, 2001; *Huang et al.*, 2004]. On 8 June 2001, seven field-aligned electron density profiles were obtained when IMAGE passed through the morning sector (MLT = 8.0) inside the plasmasphere (*L* shell between 2.22 and 3.23) within 22 min (from 20:36:57 UT to 20:58:56 UT) [*Huang et al.*, 2004]. Figure 6 shows a comparison of the DEN3D model, the seven electron density profiles along field lines and in situ electron densities. The dashed lines are the seven

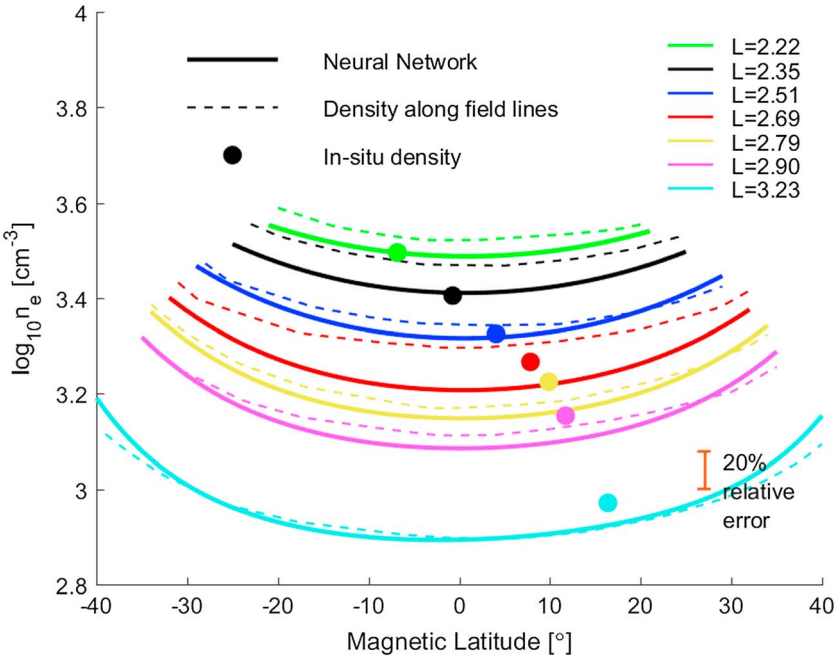

Figure 6. Comparison of the seven electron density profiles along field lines (dashed) inferred from the RPI active sounding plasmagrams from the IMAGE satellite, the modeled density profiles from the DEN3D model (solid), and the in situ densities inferred from upper hybrid resonance frequency at the same seven L shells (dots). Seven colors indicate different *L* shells of the measured field-aligned density profiles. The error bar on the bottom right corresponds to a relative error of 20%.

field-aligned density profiles from the RPI active sounding plasmagrams. Observations at seven L shells are illustrated in different colors. The solid lines show the field-aligned density profiles modeled by the DEN3D model at the same seven L shells as indicated by different colors. The solid circles are in situ electron densities inferred from upper hybrid resonance frequency at the same seven L shells. The error bar on the bottom right corresponds to a relative error of 20% ($10^{0.08}$ = 1.2). In general, good agreement has been found between the field-aligned density profiles and the DEN3D model. The agreement is extremely good at the highest L shell. At lower L shell, the measured field-aligned density profiles are higher than the DEN3D model by ~0.05 depending on different L shells. Note that these errors are still much smaller than the RMSE of the DEN3D model on the test data set (0.292), which suggests that the DEN3D model can predict these field-aligned density profiles for this specific event very well. In addition, the in situ measured densities agree very well with the neural network predictions as the in situ measurements overlap with the lines of the DEN3D modeled at most L shells. In the intermediate L shells, they are differed by ~0.05, which can be translated to a relative error of a factor of ~10% ($10^{0.05}$ = 1.12). This error is smaller than the relative error of the electron density derived from the wave measurements, which is typically close to or less than 20% [*Reinisch et al.*, 2004]. By taking this into consideration, the predictive ability of the DEN3D model on the out-of-sample observations might be better than shown here. Furthermore, it is worth noting that the DEN3D model is a global time-dependent model that works for much larger regions and under a large range of geomagnetic activity levels rather than an event-specific model. In sum, the good agreement between the two models demonstrates the capability of the DEN3D model in out-of-sample prediction.

4. Event Analysis

4.1. 1 June 2013 Storm

The DEN3D model was applied to a moderate storm that occurred on 1 June 2013. The storm sudden commencement occurs around 16 UT on 31 May when the solar wind dynamic pressure started to increase. The storm main phase started around 00 UT on 1 June when interplanetary magnetic field B_z turned southward (not shown). The geomagnetic indices *SYM-H* and *AL* (absolute values) are shown in the first panel in Figure 7.

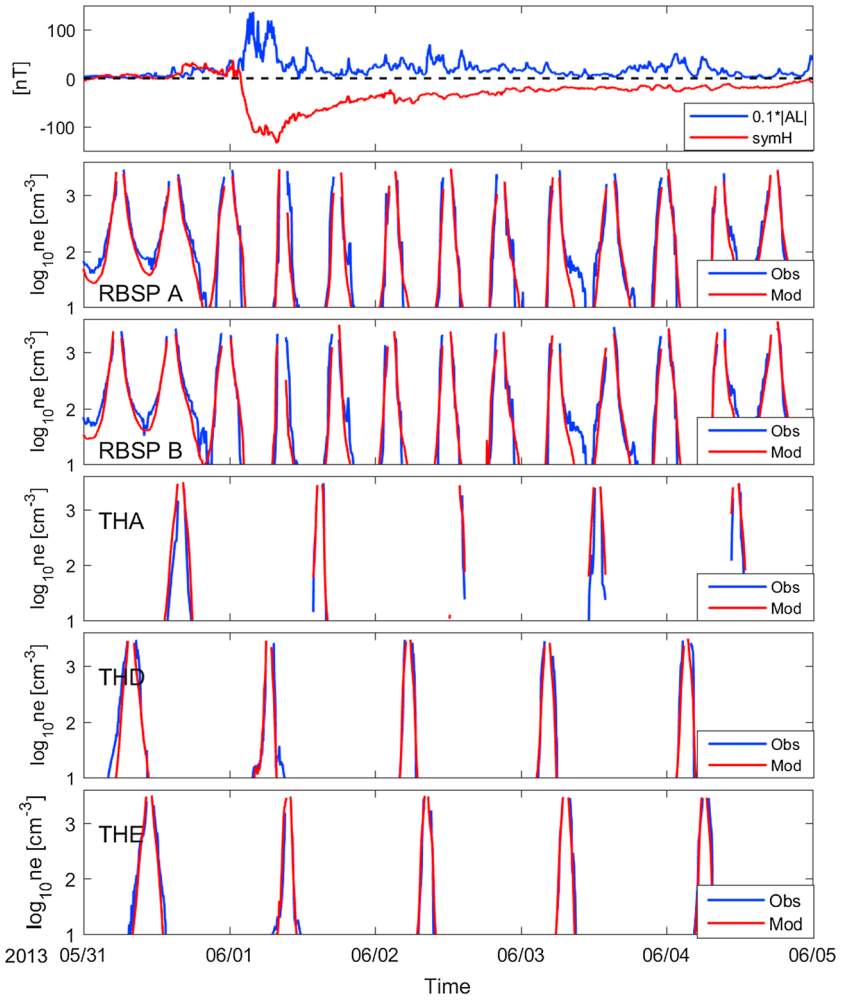

Figure 7. Comparison between the observed electron density (blue) obtained from RBSP and THEMIS satellites and the modeled values (red) by the DEN3D model. The top figure shows the *SYM-H* index (red) and the absolute values of the *AL* index (blue).

The *SYM-H* index dropped to a minimum value of −134 nT during the storm main phase, and then started to recover for the following 3 days. The comparisons between the observed and modeled electron densities obtained from RBSP and Time History of Events and Macroscale Interactions during Substorms (THEMIS) satellites are shown in the following panels. The electron density is obtained using the upper hybrid resonance frequency from the Electric and Magnetic Field Instrument Suite and Integrated Science instrument onboard RBSP [*Kurth et al.*, 2015] and inferred using spacecraft potential [*Li et al.*, 2010] from the electrostatic analyzers instrument [*McFadden et al.*, 2008] onboard THEMIS satellites [*Angelopoulos*, 2008]. It should be noted that the electron densities from RBSP and THEMIS are not included in the training of the DEN3D model. In addition, this storm event is completely out of sample from the time periods covered by the training data set. In other words, the prediction of the electron density from RBSP and THEMIS are completely out-of-sample observations. Good agreements are found between the observed and modeled electron densities during most times. The good agreements found demonstrate the predictive ability of the DEN3D on out-of-sample observations.

Given DEN3D's good performance in predicting plasma density, the dynamic variations of the electron densities on the equatorial plane and along magnetic field lines have been studied. Figure 8 shows the equatorial electron density at four different times indicated by vertical dashed lines. Before the storm (Figure 8a), the nominal plasmasphere (contour of 100 cm^{-3}, plotted as a black dashed line) was large and symmetric.

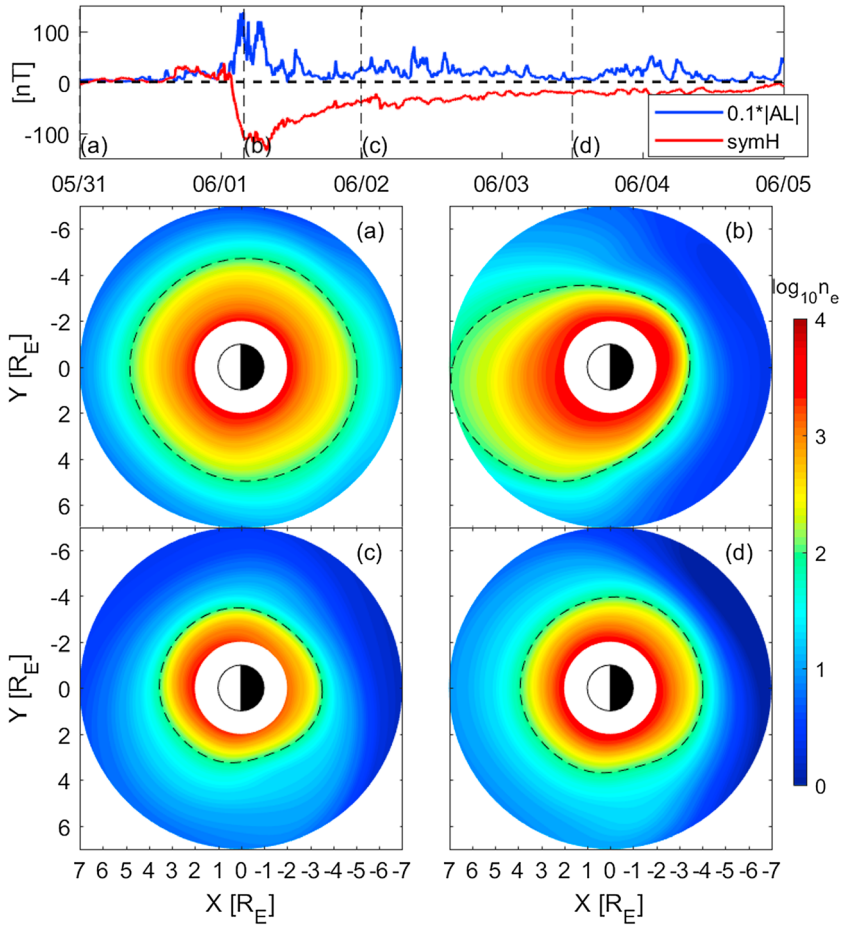

Figure 8. Overview of equatorial electron density profiles during a geomagnetic storm occurred on 1 June 2013. The top figure shows the *SYM-H* index (red) and the absolute values of the *AL* index (blue). The four contours show the equatorial density profiles modeled by the DEN3D model. The four times are indicated by the vertical dashed lines.

During the storm main phase (Figure 8b), the erosion of the plasmasphere occurred in the nightside and dawn sectors, causing the plasmapause to contract and move earthward. In the afternoon sector, the plasmasphere was extended and a plasmaspheric plume formed. The plume disappeared during the recovery phase (Figure 8c). The plasmasphere started to recover slowly during the recovery phase (Figures 8c and 8d) due to ionospheric outflow and the plasmapause gradually moved toward higher L shell.

Figure 9 shows the electron density profiles along field lines in the noon-midnight meridian plane at times (same as Figure 8) indicated by the vertical dashed lines during the same storm event. During quiet times before the storm (Figure 9a), the plasmasphere was extended. The nominal plasmapause (contour of 100 cm^{-3}, plotted as a black line) reached about 5 R_E in the nightside and dayside meridian. Around the minimum of the *SYM-H* index (Figure 9b), the electron density became depleted in the trough region on the nightside and the plasmapause contracted to L = 3.5. On the dayside, the electron density increased and the plasmapause extended to L = 7 due to the formation of the plasmaspheric plume. During the storm recovery phase (Figures 9c and 9d), plasmaspheric refilling started to take place as ionospheric outflow refilled the depleted regions in the magnetosphere. On the nightside, the electron density in the trough region started to recover and the plasmapause slowly moved outward. On the dayside, the electron density dropped and the plasmapause moved inward as the plasmaspheric plume disappeared.

Figure 10 shows the density profiles along field lines in the midnight meridian at five different *L* shells as a function of time and MLAT during the same storm event. The last panel shows the electron densities on the equator at these *L* shells. The density depletions were clearly dependent on *L* shell. The high *L* shell (*L* = 5.5) was outside the nominal plasmapause. At this *L* shell, the density depletion occurred soon after

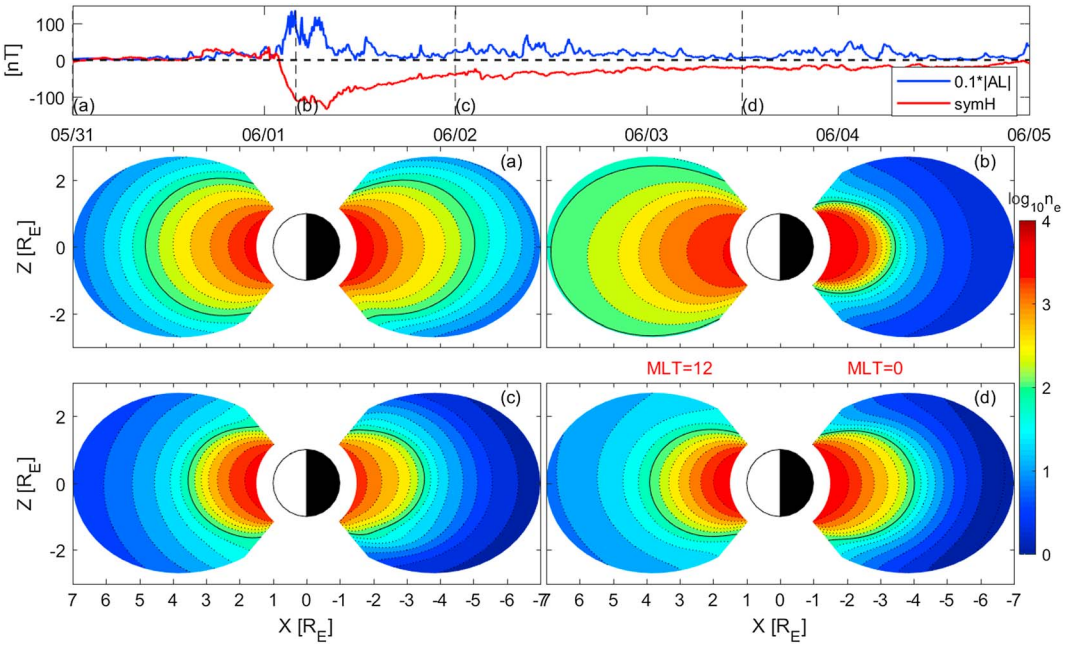

Figure 9. Overview of electron density profiles along magnetic field lines during a geomagnetic storm occurred on 1 June 2013. The top figure shows the *SYM-H* index (red) and the absolute values of the *AL* index (blue). The four contours show the field-aligned density profiles in the noon-midnight meridian plane modeled by the DEN3D model. The four times are indicated by the vertical dashed lines.

the storm sudden commencement and lasted for 4 days throughout the storm. The electron density did not recover until 5 June. The low *L* shells (*L* = 1.5 and 2.5) was inside the plasmasphere all the time. At the low *L* shells, the electron density was stable during quiet time phase since the plasmaspheric density is usually relatively constant. The electron density decreased slightly during the storm main phase and recovered 2 days later. It is interesting that the plasmaspheric density increased sometimes during the main phase, which was likely due to positive ionospheric storm effects [*Seaton*, 1956; *Prölss*, 1993]. The *L* shells (*L* = 3.5 and 4.5) were inside the plasmasphere during quiet time and outside during the storm. At the two *L* shells, the depletion lasted shorter and the recovery was quicker compared to higher *L* shell (*L* = 5.5) where the depletions lasted much longer. The electron density almost recovered by 3 June at these *L* shells, and the refilling rate was nonuniform throughout the recovery phase. Besides the major erosion and recovery, however, there were also short-term depletions which lasted for a few hours. These short-term depletions occurred not only during the recovery phase but also during quiet times. They usually coincided with substorm activity or enhanced convection as indicated by the *AL* index and were usually greater at higher *L* shells, as expected. In summary, the long-term variations in the field-aligned density profiles are consistent with the storm effects as indicated by the *SYM-H* index, while the short-term variations were seen to be modulated by the *AL* index.

5. Discussion

A time-dependent three-dimensional electron density model of the inner magnetosphere is important for a variety of applications. For example, the electron density strongly influences wave growth rates of instabilities, modulates energetic particle scattering, and affects wave excitation and propagation. Several empirical models have been developed previously to describe the plasma density in the equatorial plane and along magnetic field lines. These models provide statistically averaged densities that cannot resolve the dynamic evolution of the plasma density on short time scales of a few minutes to a few hours. To study the dynamic density variations at the equator, a time-dependent model of the equatorial electron density was recently developed using a two-layer neural network with time series of *SYM-H*, *AL*, and $F_{10.7}$ indices as input [*Bortnik et al.*, 2016; *Chu et al.*, 2017]. It succeeded in reproducing various dynamic density features on the equator such as the quiet time plasmasphere, erosion, and recovery of the plasmasphere, as well as the

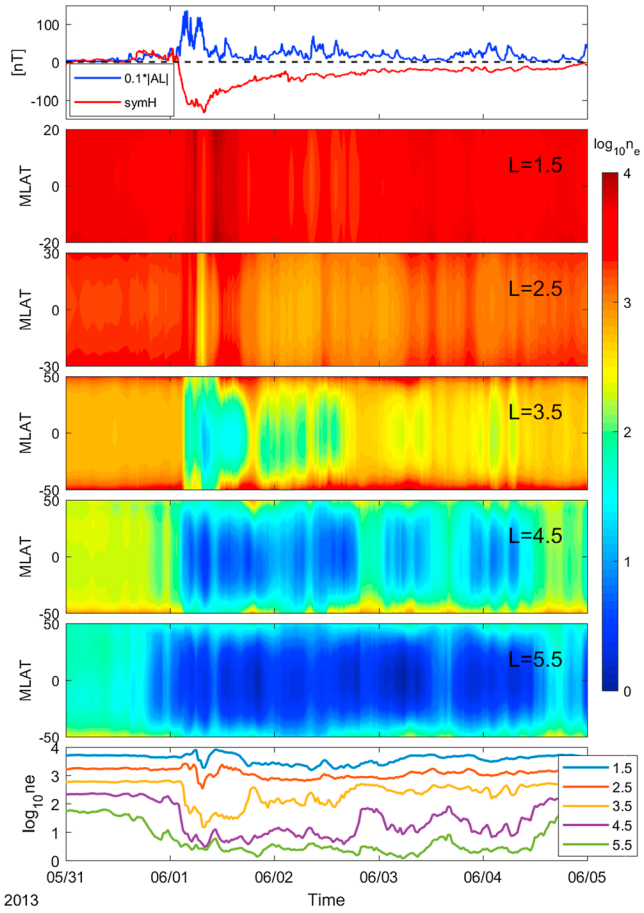

Figure 10. Temporal evolutions of the electron density along field lines in the midnight meridian at five *L* shells (from *L* = 1.5 to *L* = 5.5) during a storm on 1 June 2013. The geomagnetic indices (*SYM-H* and *AL*) are shown in the top figure. The electron densities on the equator at five *L* shells are illustrated as line plot in the last panel.

plume formation. In this follow-up study, we developed a three-dimensional dynamic electron density (DEN3D) model using data from both equatorial and polar-orbiting satellites. As a time-dependent and history-dependent model, it can be used to study the temporal variations of the field-aligned density profiles.

The neural network model is a generic and convenient way to perform nonlinear statistical modeling, and it offers a number of advantages over conventional empirical statistical fitting. First of all, empirical statistical methods are usually fitted using very simple equations, which are usually prone to under fitting. For example, the equatorial plasma density has been assumed to vary with *L* shells in a form both power law and exponential functions, and the field-aligned density has been assumed to follow a power law or exponential or composite functions. However, the dynamic features of the plasma density evolution are highly complex, involving dependences on the current level of geomagnetic activity and its past history (whether during the storm main phase or recovery phase), distance from the Earth (*L* shells), distance from the magnetic equator (magnetic latitude), and whether the observation is on the dayside or nightside or in a plasmaspheric plume (MLT asymmetry). These dependences are not all included in these equations, thus, result in under fitting in the empirical models. Second, these dependences are presently well understood and implementing them analytically requires a number of simplifying assumptions that may inadvertently suppress important physical interactions. Such assumptions can be avoided by using a neural network approach. In addition, empirical models also usually require assumptions about the observations, which are not required for a neural network model. For instance, the parameter α in the field-aligned density distribution is inferred from observations by a polar-orbiting satellite crossing the same *L* shell at two points under the assumption that there is no MLT or temporal changes in the electron density [*Goldstein et al.*, 2001; *Denton et al.*, 2002a, 2002b]. Such assumptions are not required in the neural network approach either. The neural network model has its disadvantages too, including the need for greater computational power, a larger amount of observations and the additional effort to decipher a nonintuitive model.

The DEN3D model was shown to have excellent capability not only in reproducing the observations but also in predicting out-of-sample measurements. Although the neural network we used here is relatively simple, the correlation coefficients on the whole data set are as high as 0.954, which means that it can reproduce r^2 = ~91.1% of the observed variability. The correlation coefficient is 0.9545, and the RMSE is 0.292 on the test data set (which was not used as input to the DEN3D model). This suggests that our DEN3D model has the ability to predict out-of-sample observations within error of a factor of 2 ($10^{0.292}$ = 1.96). Its ability to predict out-of-sample observations has been validated by comparing it with seven field-aligned density profiles

inferred from the RPI active sounding plasmagrams within 22 min on 8 June 2001. These were not used in the DEN3D training and thus can be used as an out-of-sample data set. The agreement between the DEN3D model and field-aligned density profiles is generally good, where the relative error was about 10% ($10^{0.05}$ = 1.12). Furthermore, the in situ measured electron densities during this event were also well predicted by the DEN3D model at the same *L* shells and latitudes, with relative errors less than 10% ($10^{0.05}$ = 1.12) at most L shells. In addition, its ability to predict out-of-sample observations has also been validated by the good agreement between the modeled and observed densities from RBSP and THEMIS during a storm which occurred on 1 June 2013. These were also not included in the training of the DEN3D model and are thus independent out-of-sample data sets. We have therefore adequately demonstrated that the DEN3D model has a good prediction capability on out-of-sample observations.

Given DEN3D's good performance in predicting the structure and evolution of the inner magnetospheric plasma density globally, the salient features of the data can be examined to gain further insight on the physics. For instance, one of the most important applications is to provide time-dependent three-dimensional distributions of the electron density at locations and times that spacecraft observations are not available. DEN3D is able to convert sparse spacecraft observations taken over a long period of time into a dense coverage taken at any given time instant. In such a way, it can be used to discover potentially important physics that is missing from physics-based models by comparing DEN3D's modeled values to physics-based models' outputs. In this study, the field-aligned density profiles in the noon-midnight meridian have been calculated for a moderate storm on 1 June 2013. It was found that the plasmaspheric depletion during this storm is consistent with the storm effects as indicated by the *SYM-H* index, while the short-term variations were modulated by the *AL* index as well. A possible explanation is that the plasmaspheric dynamics is also controlled by magnetospheric processes such as substorm injections, enhanced convection, or subauroral polarization streams [*Goldstein et al*., 2003]. Implementing these magnetospheric processes in physics-based simulations of the plasmasphere is important in studying plasmaspheric dynamics (such as SAMI model [*Huba and Krall*, 2013; *Krall and Huba*, 2013]).

Using the DEN3D model, the temporal variations of the plasma density, or the plasmaspheric refilling rates dn_e/dt, can be studied. It should be noted that transverse magnetic field line motion of the plasma is not considered in the calculation of the refilling rates because the physical process is difficult to be incorporated in an empirical plasma density model. In the past, the plasmaspheric refilling rates were calculated using observations from successive orbits during a storm. Due to the limitation of data availability, the refilling rates were usually assumed to be constant over a few days and to satisfy a specific functional form of L shell, e.g., $dn_e/dt = a^* 10^{b^* L}$ [*Denton et al*., 2012; *Krall et al*., 2016]. This function implies that the refilling rates increase monotonically approaching the Earth. In this study, we find that the density variations are very complex and not uniform throughout the storm recovery phase. For instance, since the density variations are modulated by both the *SYM-H* and *AL* indices, the refilling rates also depend on both indices rather than being constant values throughout storms. The speed of the depletion and the refilling depends on the strength of the corresponding geomagnetic activity.

Our DEN3D model could be immensely useful for space weather, for the initial setup of various simulations, and for other applications such as the dependence of plasmaspheric erosion and refilling on ionospheric and magnetospheric processes. In future studies, we will improve the plasma density model by including more observations from missions such as the Van Allen Probes, ARASE, Cluster, and from low-altitude spacecraft.

6. Summary

We present a three-dimensional dynamic electron density (DEN3D) model in the inner magnetosphere using a neural network approach. DEN3D is both time- and history-dependent as it takes time series of solar and geomagnetic indices as inputs. It can not only reproduce the observed electron density with a high correlation coefficients of 0.95 but also predict independent out-of-sample data with error less than a factor of 2. Its predictive ability is tested on seven density profiles along field lines on 8 June 2001 from IMAGE and on in situ observations from RBSP and THEMIS during a geomagnetic storm occurred on 1 June 2013.

Given its good performance in predicting plasma density at any time and location, DEN3D is applied to the storm on 1 June 2013 to study the dynamic variations of the electron density. We show that DEN3D

successfully reproduced various well-known dynamic features in three dimensions, such as plasmaspheric erosion and recovery, as well as the plume formation during the storm that occurred on 1 June 2013. It was found that the long-term variations of the electron density are consistent with the storm effects measured by the *SYM-H* index, while the short-term variations were seen to be modulated by the *AL* index that indicates substorm activity or enhanced convection. Therefore, the plasmaspheric refilling is not monotonic and is more complex than expected from previous studies, a topic of importance and deserving of future studies in conjunction with multispacecraft in situ observations or imaging measurements.

Acknowledgments
The authors would like to gratefully acknowledge NASA grant NNX14AN85G and AFOSR grant FA9550-15-1-0158. Wen Li would like to acknowledge the National Science Foundation grant of AGS-1723342. Richard Denton would like to acknowledge the NSF grant of AGS-1105790. Chao Yue gratefully acknowledges support from NASA Living With a Star Jack Eddy Postdoctoral Fellowship Program, administered by the UCAR Visiting Scientist Programs. The authors would like to thank Ivan Galkin for providing electron density along field lines from active RPI active sounding plasmagrams onboard IMAGE. The authors would like to thank Paul O'Brien and Robert McPherron for helpful discussions. We would like to acknowledge the NSSDC Omniweb for the geomagnetic activity indices (ftp://spdf.gsfc.nasa.gov/pub/data/omni/omni_cdaweb/) used in this study.

References

Anderson, R. R., D. A. Gurnett, and D. L. Odem (1992), CRRES plasma wave experiment, *J. Spacecr. Rockets*, *29*(4), 570–573, doi:10.2514/3.25501.

Angelopoulos, V. (2008), The THEMIS mission, *Space Sci. Rev.*, *141*(1), 5–34, doi:10.1007/s11214-008-9336-1.

Bortnik, J., R. M. Thorne, N. P. Meredith, and O. Santolik (2007), Ray tracing of penetrating chorus and its implications for the radiation belts, *Geophys. Res. Lett.*, *34*, L15109, doi:10.1029/2007GL030040.

Bortnik, J., W. Li, R. M. Thorne, and V. Angelopoulos (2016), A unified approach to inner magnetospheric state prediction, *J. Geophys. Res. Space Physics*, *121*, 2423–2430, doi:10.1002/2015JA021733.

Burch, J. L., et al. (2001), Views of Earth's magnetosphere with the IMAGE satellite, *Science*, *291*(5504), 619–624, doi:10.1126/science.291.5504.619.

Carpenter, D. L. (1966), Whistler studies of the plasmapause in the magnetosphere: 1. Temporal variations in the position of the knee and some evidence on plasma motions near the knee, *J. Geophys. Res.*, *71*(3), 693–709, doi:10.1029/JZ071i003p00693.

Carpenter, D. L., and R. R. Anderson (1992), An ISEE/whistler model of equatorial electron-density in the magnetosphere, *J. Geophys. Res.*, *97*(A2), 1097–1108, doi:10.1029/91JA01548.

Chu, X., R. L. McPherron, T.-S. Hsu, and V. Angelopoulos (2015), Solar cycle dependence of substorm occurrence and duration: Implications for onset, *J. Geophys. Res. Space Physics*, *120*, 2808–2818, doi:10.1002/2015JA021104.

Chu, X. N., J. Bortnik, W. Li, Q. Ma, V. Angelopoulos, and R. M. Thorne (2017), Erosion and refilling of the plasmasphere during a geomagnetic storm modeled by a neural network, *J. Geophys. Res. Space Physics*, *122*, 7118–7129, doi:10.1002/2017JA023948.

Darrouzet, F., J. De Keyser, P. M. E. Décréau, F. El Lemdani-Mazouz, and X. Vallières (2008), Statistical analysis of plasmaspheric plumes with Cluster/WHISPER observations, *Ann. Geophys.*, *26*(8), 2403–2417, doi:10.5194/angeo-26-2403-2008.

Darrouzet, F., J. de Keyser, and V. Pierrard (2009), *The Earth's Plasmasphere: A CLUSTER and IMAGE Perspective*, Springer Science & Business Media, Springer, New York.

Dent, Z. C., I. R. Mann, J. Goldstein, F. W. Menk, and L. G. Ozeke (2006), Plasmaspheric depletion, refilling, and plasmapause dynamics: A coordinated ground-based and IMAGE satellite study, *J. Geophys. Res.*, *111*, A03205, doi:10.1029/2005JA011046.

Denton, R. E., J. Goldstein, and J. D. Menietti (2002a), Field line dependence of magnetospheric electron density, *Geophys. Res. Lett.*, *29*(24), 2205, doi:10.1029/2002GL015963.

Denton, R. E., J. Goldstein, J. D. Menietti, and S. L. Young (2002b), Magnetospheric electron density model inferred from Polar plasma wave data, *J. Geophys. Res.*, *107*(A11), 1386, doi:10.1029/2001JA009136.

Denton, R. E., J. D. Menietti, J. Goldstein, S. L. Young, and R. R. Anderson (2004), Electron density in the magnetosphere, *J. Geophys. Res.*, *109*, A09215, doi:10.1029/2003JA010245.

Denton, R. E., K. Takahashi, I. A. Galkin, P. A. Nsumei, X. Huang, B. W. Reinisch, R. R. Anderson, M. K. Sleeper, and W. J. Hughes (2006), Distribution of density along magnetospheric field lines, *J. Geophys. Res.*, *111*, A04213, doi:10.1029/2005JA011414.

Denton, R. E., Y. Wang, P. A. Webb, P. M. Tengdin, J. Goldstein, J. A. Redfern, and B. W. Reinisch (2012), Magnetospheric electron density long-term (>1 day) refilling rates inferred from passive radio emissions measured by IMAGE RPI during geomagnetically quiet times, *J. Geophys. Res.*, *117*, A03221, doi:10.1029/2011JA017274.

Foster, J. C., P. J. Erickson, A. J. Coster, S. Thaller, J. Tao, J. R. Wygant, and J. W. Bonnell (2014), Storm time observations of plasmasphere erosion flux in the magnetosphere and ionosphere, *Geophys. Res. Lett.*, *41*, 762–768, doi:10.1002/2013GL059124.

Gallagher, D. L., P. D. Craven, and R. H. Comfort (2000), Global core plasma model, *J. Geophys. Res.*, *105*(A8), 18,819–18,833, doi:10.1029/1999JA000241.

Goldstein, J., R. E. Denton, M. K. Hudson, E. G. Miftakhova, S. L. Young, J. D. Menietti, and D. L. Gallagher (2001), Latitudinal density dependence of magnetic field lines inferred from Polar plasma wave data, *J. Geophys. Res.*, *106*(A4), 6195–6201, doi:10.1029/2000JA000068.

Goldstein, J., B. R. Sandel, M. R. Hairston, and P. H. Reiff (2003), Control of plasmaspheric dynamics by both convection and sub-auroral polarization stream, *Geophys. Res. Lett.*, *30*(24), 2243, doi:10.1029/2003GL018390.

Goldstein, J., B. R. Sandel, M. F. Thomsen, M. Spasojević, and P. H. Reiff (2004), Simultaneous remote sensing and in situ observations of plasmaspheric drainage plumes, *J. Geophys. Res.*, *109*, A03202, doi:10.1029/2003JA010281.

Grebowsky, J. M. (1970), Model study of plasmapause motion, *J. Geophys. Res.*, *75*(22), 4329–4333, doi:10.1029/JA075i022p04329.

Gurnett, D. A., F. L. Scarf, R. W. Fredricks, and E. J. Smith (1978), The ISEE-1 and ISEE-2 plasma wave investigation, *IEEE Trans. Geosci. Electron.*, *16*(3), 225–230, doi:10.1109/TGE.1978.294552.

Gurnett, D. A., et al. (1995), The Polar plasma wave instrument, *Space Sci. Rev.*, *71*(1), 597–622, doi:10.1007/bf00751343.

Huang, X., B. W. Reinisch, P. Song, J. L. Green, and D. L. Gallagher (2004), Developing an empirical density model of the plasmasphere using IMAGE/RPI observations, *Adv. Space Res.*, *33*(6), 829–832, doi:10.1016/j.asr.2003.07.007.

Huba, J., and J. Krall (2013), Modeling the plasmasphere with SAMI3, *Geophys. Res. Lett.*, *40*, 6–10, doi:10.1029/2012GL054300.

Kersley, L., and J. A. Klobuchar (1980), Storm associated protonospheric depletion and recovery, *Planet. Space Sci.*, *28*(5), 453–458, doi:10.1016/0032-0633(80)90026-4.

Krall, J., and J. D. Huba (2013), SAMI3 simulation of plasmasphere refilling, *Geophys. Res. Lett.*, *40*, 2484–2488, doi:10.1002/grl.50458.

Krall, J., J. D. Huba, V. K. Jordanova, R. E. Denton, T. Carranza, and M. B. Moldwin (2016), Measurement and modeling of the refilling plasmasphere during 2001, *J. Geophys. Res. Space Physics*, *121*, 2226–2248, doi:10.1002/2015JA022126.

Kurth, W. S., S. De Pascuale, J. B. Faden, C. A. Kletzing, G. B. Hospodarsky, S. Thaller, and J. R. Wygant (2015), Electron densities inferred from plasma wave spectra obtained by the Waves instrument on Van Allen Probes, *J. Geophys. Res. Space Physics*, *120*, 904–914, doi:10.1002/2014JA020857.

Lemaire, J., K. Gringauz, V. Bassolo, and D. Carpenter (1998), *The Earth's Plasmasphere*, Cambridge Univ. Press, Cambridge, U. K., and New York.
Li, W., R. M. Thorne, J. Bortnik, Y. Nishimura, V. Angelopoulos, L. Chen, J. P. McFadden, and J. W. Bonnell (2010), Global distributions of suprathermal electrons observed on THEMIS and potential mechanisms for access into the plasmasphere, *J. Geophys. Res.*, *115*, A00J10, doi:10.1029/2010JA015687.
McFadden, J. P., C. W. Carlson, D. Larson, M. Ludlam, R. Abiad, B. Elliott, P. Turin, M. Marckwordt, and V. Angelopoulos (2008), The THEMIS ESA plasma instrument and in-flight calibration, *Space Sci. Rev.*, *141*(1–4), 277–302, doi:10.1007/s11214-008-9440-2.
Millan, R. M., and R. M. Thorne (2007), Review of radiation belt relativistic electron losses, *J. Atmos. Sol. Terr. Phys.*, *69*(3), 362–377, doi:10.1016/j.jastp.2006.06.019.
Nishida, A. (1966), Formation of plasmapause, or magnetospheric plasma knee, by the combined action of magnetospheric convection and plasma escape from the tail, *J. Geophys. Res.*, *71*(23), 5669–5679, doi:10.1029/JZ071i023p05669.
O'Brien, T. P., and M. B. Moldwin (2003), Empirical plasmapause models from magnetic indices, *Geophys. Res. Lett.*, *30*(4), 1152, doi:10.1029/2002GL016007.
Ober, D. M., J. L. Horwitz, M. F. Thomsen, R. C. Elphic, D. J. McComas, R. D. Belian, and M. B. Moldwin (1997), Premidnight plasmaspheric "plumes", *J. Geophys. Res.*, *102*(A6), 11,325–11,334, doi:10.1029/97JA00562.
Ozhogin, P., J. Tu, P. Song, and B. W. Reinisch (2012), Field-aligned distribution of the plasmaspheric electron density: An empirical model derived from the IMAGE RPI measurements, *J. Geophys. Res.*, *117*, A06225, doi:10.1029/2011JA017330.
Prölss, G. W. (1993), Common origin of positive ionospheric storms at middle latitudes and the geomagnetic activity effect at low latitudes, *J. Geophys. Res.*, *98*(A4), 5981–5991, doi:10.1029/92JA02777.
Reinisch, B. W., et al. (2000), The radio plasma imager investigation on the IMAGE spacecraft, *Space Sci. Rev.*, *91*(1–2), 319–359, doi:10.1023/A:1005252602159.
Reinisch, B. W., X. Huang, P. Song, G. S. Sales, S. F. Fung, J. L. Green, D. L. Gallagher, and V. M. Vasyliunas (2001), Plasma density distribution along the magnetospheric field: RPI observations from IMAGE, *Geophys. Res. Lett.*, *28*(24), 4521–4524, doi:10.1029/2001GL013684.
Reinisch, B. W., X. Huang, P. Song, J. L. Green, S. F. Fung, V. M. Vasyliunas, D. L. Gallagher, and B. R. Sandel (2004), Plasmaspheric mass loss and refilling as a result of a magnetic storm, *J. Geophys. Res.*, *109*, A01202, doi:10.1029/2003JA009948.
Reinisch, B. W., M. B. Moldwin, R. E. Denton, D. L. Gallagher, H. Matsui, V. Pierrard, and J. N. Tu (2009), Augmented empirical models of plasmaspheric density and electric field using IMAGE and CLUSTER data, *Space Sci. Rev.*, *145*(1–2), 231–261, doi:10.1007/s11214-008-9481-6.
Sandel, B. R., and M. H. Denton (2007), Global view of refilling of the plasmasphere, *Geophys. Res. Lett.*, *34*, L17102, doi:10.1029/2007GL030669.
Seaton, M. J. (1956), A possible explanation of the drop in F-region critical densities accompanying major ionospheric storms, *J. Atmos. Terr. Phys.*, *8*(1–2), 122–124, doi:10.1016/0021-9169(56)90102-7.
Sheeley, B. W., M. B. Moldwin, H. K. Rassoul, and R. R. Anderson (2001), An empirical plasmasphere and trough density model: CRRES observations, *J. Geophys. Res.*, *106*(A11), 25,631–25,641, doi:10.1029/2000JA000286.
Thorne, R. M., et al. (2013), Rapid local acceleration of relativistic radiation-belt electrons by magnetospheric chorus, *Nature*, *504*(7480), 411–414, doi:10.1038/nature12889.
Tsyganenko, N. A., and M. I. Sitnov (2005), Modeling the dynamics of the inner magnetosphere during strong geomagnetic storms, *J. Geophys. Res.*, *110*, A03208, doi:10.1029/2004JA010798.
Tu, J. N., P. Song, B. W. Reinisch, J. L. Green, and X. Q. Huang (2006), Empirical specification of field-aligned plasma density profiles for plasmasphere refilling, *J. Geophys. Res.*, *111*, A06216, doi:10.1029/2005JA011582.

Erratum

In the originally published version of this article, a grant was omitted from the Acknowledgments. The article has been updated to acknowledge the grant, and the present version may be considered the authoritative version of record.